Available online at www.sciencedirect.com

ScienceDirect

Ceramics International 40 (2014) 4039–4053

CERAMICS INTERNATIONAL

www.elsevier.com/locate/ceramint

Iron oxide supported sulfated TiO_2 nanotube catalysts for NO reduction with propane

Katabathini Narasimharao*, Maqsood Ahmad Malik, Mohamed M. Mokhtar, Sulaiman N. Basahel, Shaeel A. Al-Thabaiti

Chemistry Department, Faculty of Science, King Abdulaziz University, Jeddah 21589, Saudi Arabia

Received 10 May 2013; received in revised form 16 July 2013; accepted 13 August 2013
Available online 20 August 2013

Abstract

Sulfated TiO_2 nanotubes and a series of iron oxide loaded sulfated TiO_2 nanotubes catalysts with different iron oxide loadings (1 wt%, 3 wt%, 5 wt% and 7 wt%) were prepared and calcined at 400 °C. The physico-chemical properties of the catalysts were studied by using XRD, N_2-physisorption, Raman spectroscopy, SEM-EDX, TEM, XPS, and pyridine adsorption using FTIR and H_2-TPR techniques. It was observed that iron oxide was highly dispersed on the sulfated TiO_2 nanotube support due to its strong interaction. The activity of these catalysts in the catalytic removal of NO with propane was also studied in the temperature range of 300–500 °C. Highest activity (90% NO conversion) was observed with 5 wt% iron oxide supported on sulfated TiO_2 catalyst at 450 °C. Selective catalytic reduction of NO activity of the catalysts was correlated with iron oxide loading, reducibility, and the Brönsted and Lewis acid sites of the catalysts. The catalyst also showed good stability under studied reaction conditions that no deactivation was observed during the 50 h of reaction.

© 2013 Elsevier Ltd and Techna Group S.r.l. All rights reserved.

Keywords: B. Electron microscopy; B. Porosity; B. X-ray methods; Nanomaterials: chemical preparation

1. Introduction

The removal of NO_x from diesel exhaust and lean-burn processes is very important due to its dangerous impact on the environment resulting in acid rains, smog, as well as visibility impairment and human health problems such as lung infections and respiratory allergies [1]. One of the solutions to remove this toxic NO gas is by selective catalytic reduction of NO_x using hydrocarbons (HC-SCR). This is an attractive method for the purification of exhaust gases emitted from mobile sources where the use of NH_3 as reducing agent is not feasible. Many studies appeared in the literature on the utilization of light hydrocarbons (C_1–C_4) as reduction agent, in particular methane [2], ethylene [3], propene [4] and propane [5].

Titanium dioxide (TiO_2) has been widely employed as a support for a commercial SCR catalyst on which the active species, V_2O_5, WO_3 and/or MoO_3 are well dispersed [6]. TiO_2 alone showed some NO removal activity and selectivity to N_2 at a reaction temperature around 400 °C [7]. TiO_2 nanotubes possess remarkably superior catalytic properties in many applications compared with other forms of nanocrystalline TiO_2 because of their high surface area and charge transport property. Therefore, the synthesis of TiO_2 nanotubes has been recognized as an important research topic. Various methods for the synthesis of TiO_2 nanotubes have been developed in recent years, including anodic oxidation [8], template synthesis [9], and hydrothermal synthesis [10]. The hydrothermal synthesis method has become one of the most promising techniques because of its ability for large area growth of nanotubes and simplicity [11].

It was reported that sulfated oxides such as ZrO_2, TiO_2, SnO_2 and Fe_2O_3 are strong solid acid catalysts that have possessed high thermal stability, strong acidity and high catalytic activities in many environmentally friendly reactions [12]. Sulfated TiO_2 or its mixture with other oxide such as ZrO_2 has been found to be effective catalyst for many reactions such as isomerization, alkylation, Friedel–Crafts acylation, esterification, photocatalytic

---

*Corresponding author. Tel.: +966 538638994; fax: +966 26952292.
E-mail address: katabathini@yahoo.com (K. Narasimharao).

0272-8842/$ - see front matter © 2013 Elsevier Ltd and Techna Group S.r.l. All rights reserved.
http://dx.doi.org/10.1016/j.ceramint.2013.08.058

oxidation and SCR of NO_x [13]. It has been reported that the sulfate species on the surface of support is favorable for NO removal reaction [14]. The sulfate species on the support surface affects not only the structure of active species but also the catalyst acidity which plays an important role for conversion of NO_x SCR reaction [15].

Long et al. [16] reported that Fe-exchanged TiO_2-pillared clay was more active than V_2O_5-based catalysts for SCR of NO by NH_3. The authors also observed that SCR activity can be improved by 50% after sulfation of catalyst in presence of SO_2 and O_2 at 450 °C. Zhang et al. [17] studied SCR of NO with propane in excess oxygen over Ni–ZrO_2 and sulfated Ni–ZrO_2. It was found that sulfated Ni–ZrO_2 catalyst showed higher activity for the SCR of NO with propane than that of Ni–ZrO_2. The authors also observed that generation of strong Brönsted and Lewis acid sites promoted the dispersion of the Ni species, which lead to higher NO conversion and propane efficiency in SCR of NO. Bayleta et al. [18] investigated the NO_x reduction activity over different CeO_2 supported sulfated TiO_2 catalysts, which indicated that the SCR of NO_x activity increased with sulfation.

Holbrook et al. [19] studied the SCR of NO by n-decane over sulfated TiO_2 catalysts. The authors reported that the sulfate species (SO_4^{2-}, SO_3^{2-}) were stable up to 600 °C under inert atmosphere, whereas the sulfate species were released from the catalysts at around 400 °C under HC-SCR reaction conditions. Very recently Chen et al. [20] synthesized titanates with different morphologies including nanotubes and utilized them as supports for SCR of NO. Their experimental results revealed that CeO_2 supported TiO_2 nanotube samples showed very good catalytic performance.

In the present paper, we want to report synthesis of acidic iron oxide supported sulfated TiO_2 nanotube catalysts with different iron oxide loadings, their characterization and application in SCR of NO using propane as reducing agent. To best of our knowledge, the application of sulfated iron oxide supported TiO_2 nanotube catalysts for the aforementioned reaction has not been previously reported.

2. Experimental

2.1. Chemicals and gases

TiO_2 anatase (P25, Degussa AG, Germany), NaOH pellets, $Fe(NO_3)_3$ hexahydrate, and H_2SO_4 (S.D. Fine-Chem. Ltd, A. R. grade) were procured from commercial suppliers and used as received. Double distilled water was used in the preparation. NO_x, nitrogen, helium and air gases had a purity of 99.9%.

2.2. Preparation of catalysts

The preparation of TiO_2 nanotubes was based on the alkaline hydrothermal method proposed by Kasuga et al. [10]; typically, 6 g of commercial TiO_2 powder was dispersed in 120 mL of 10 M NaOH solution. The resulting suspension was stirred for 30 min, and transferred into a Teflon-lined stainless steel autoclave, sealed, and maintained at 130 °C for 48 h. The resulting material was filtered, neutralized with 0.1 M HCl solution and washed with deionized water for five times to remove the NaCl formed. The material was dried in air at 100 °C for 12 h and finally calcined in air at 400 °C for 5 h.

To prepare sulfated TiO_2 nanotubes, the dried TiO_2 nanotubes powder was suspended in 0.5 M H_2SO_4 solution using the ratio of 1.0 g of powder to 15 mL of the H_2SO_4 solution. The resulting sulfated TiO_2 powder was filtered and dried at 110 °C for 24 h and then calcined at 400 °C for 5 h to obtain the final sulfated TiO_2 nanotubes.

Conventional impregnation method was used to prepare iron oxide supported sulfated TiO_2 nanotube catalysts. Calculated amount of sulfated TiO_2 nanotube powder was added to the solution containing ferric nitrate nonahydrate corresponded to 1.0, 3.0, 5.0 and 7.0 wt% of iron oxide. The resultant cake was stirred for 4 h, washed with distilled water, dried and calcined at 500 °C for 5 h. The calcined materials were annotated as follows: xFeSTiO$_2$, where $x=1$, 3, 5 and 7 wt% of iron oxide and S represents for sulfation.

2.3. Characterization of catalysts

The phase identification for the catalysts was performed using a Philips X'pert pro diffractometer, operated at 40 kV and 40 mA, using CuK$_\alpha$ radiation, in the 2θ range from 2° to 100° in steps of 0.02°, with a sampling time of one second/step. The average crystallite size was calculated using Scherrer's equation:

$$D_{\mathrm{hkl}} = K\lambda/(B_{\mathrm{hkl}}\cos\theta) \qquad (1)$$

where D_{hkl} is the average crystallite size of the phase under investigation, K is Scherrer's constant (0.89), λ is the wavelength of the X-ray beam used (1.54056 Å), B_{hkl} is the full width at half maximum (FWHM) of the analyzed diffraction peak (101) and θ is the diffraction angle.

SEM-EDX measurements were carried out using a JEOL JSM840A fitted with an Oxford Instruments INCA energy dispersive analytical system. Each of the powder samples was attached to an aluminum block using double sided carbon tape. The samples were then coated in gold to make them conductive and compatible with the SEM/EDX technique. An SEM image (20×) was acquired of each of the powders and EDX analysis of 3 points of each sample was performed. Each of the samples was imaged and then subjected to EDX analysis. A Philips CM200FEG microscope, 200 kV, equipped with a field emission gun was used for TEM and HRTEM analyses. For the preparation of a sample for TEM, a suspension containing about 1 mg adsorbent/ml of ethanol was prepared and sonicated for 10 min. A few drops of the suspension were placed on a hollow copper grid coated with a carbon film. The coefficient of spherical aberration was $Cs=1.35$ mm. The information limit was better than 0.18 nm. High-resolution images with a pixel size of 0.044 nm were taken with a CCD camera.

The Raman spectra of samples were measured with a Bruker Equinox 55 FT-IR spectrometer equipped with an FRA106/S

FT-Raman module and a liquid nitrogen cooled Ge detector using the 1064 nm line of a Nd:YAG laser with an output laser power of 200 mW.

The samples were subjected to a pyridine adsorption analysis in a Perkin-Elmer Spectrum 100 FTIR spectrometer. The analysis was carried out over a catalyst disk which was treated under vacuum for 5 h. Later, the sample was treated with pyridine vapor and finally heated at 100 °C under vacuum for 30 min. FTIR spectra were collected at room temperature. The amount of Brönsted and Lewis acid sites was calculated via integration of the area of the absorption bands showing the maximum values of intensity at 1450 and 1550 cm^{-1}, respectively. Integrated absorbance of each band was obtained using the appropriate software by applying the corresponding extinction coefficient and normalized by the weight of the samples.

The textural properties of the prepared samples were determined from N_2 gas adsorption/desorption isotherm measurements at −196 °C using Autosorb-1-MP system (Quantachrome, USA). Prior to measurement, each sample was degassed for 6 h at 150 °C. The specific surface area, S_{BET}, was calculated by applying the Brunauer–Emmett–Teller (BET) equation. The average pore radius was estimated from the relation $2Vp/S_{BET}$, where Vp is the total pore volume (at $P/P^0=0.975$). Pore size distribution over the mesopore range was generated by the Barrett–Joyner–Halenda (BJH) analysis of the desorption branches, and the values for the average pore size were calculated. The reducibility of each catalyst was determined by H_2-temperature-programmed reduction (H_2-TPR) technique using a Quantachrome CHEMBET 3000 instrument. Typically, a sample of 50 mg was first pretreated in helium (He) gas at 120 °C for 2 h, then cooled to 30 °C and subsequently the sample was reduced with H_2. The TPR profiles were recorded with a thermal conductivity detector at a heating rate of 10 °C min^{-1} from 30 °C to 500 °C.

2.4. SCR of NO with propane

The SCR catalytic activity experiments were carried out in a catalytic reaction unit, which consists of the feed gas system, a three-zone furnace controlled by PID controllers and mass flow controllers. All experiments took place in a stainless steel flow reactor. The catalyst was placed in the middle of two zones of inert material (quartz). The loading was 1 g of catalyst and gas feed for the reaction was composed of 1000 ppm NO and 1000 ppm C_3H_8, 5.0 vol% O_2, with He as the balance. The total gas flow rate was 60 mL/min (corresponding to GHSV = 3600 h^{-1}). All lines prior to the reactor were heated at 120 °C to avoid any condensation. Samples from the exit gas stream were analyzed online to identify the gas products. The nitrogen oxides (NO, N_2O and NO_2), propane, CO_2 and CO were continuously analyzed by an FTIR spectrometer (Bruker Tensor) equipped with a heated, low volume multiple-path gas cell (2 m). The spectra were collected three times for average after 60–120 min when the SCR process reached a steady state. It took 6–8 h to conduct each SCR reaction study, during which no degradation characteristic of catalysts was observed.

3. Results and discussion

3.1. Powder X-ray diffraction

XRD analysis was used to identify the phase structure and determine the crystallite size of the samples. Fig. 1 presents the XRD patterns of all the samples calcined at 400 °C. The XRD pattern of TiO_2 raw material also included for comparison and this sample is highly crystalline and showed peaks at 2θ values of 25.4, 37.6, 48.3, 54.2 and 62.7 corresponding to the anatase phase (101), (004), (200), (211) and (204) crystal planes, respectively.

The major difference in the XRD patterns between the TiO_2 raw material and the TiO_2 nanotubular sample (Fig. 1) is the appearance of a new and strong broad peak around $2\theta=9.5°$ for the nanotube product, which does not exist for the TiO_2 raw material. The main peaks in the pattern of TiO_2 nano sample can be found at 9.5°, 24.3°, 28.7° and 48.3°. These peaks are indexed to (200), (110), (211) and (020) planes of $Na_2Ti_3O_7$ structure, which possesses a monoclinic unit cell [JCPDS no. 00-031-1329]. This observation is consistent with the previous reports [21].

The XRD patterns of sulfated TiO_2 nanotubes and samples with 1–7 wt% iron oxide loading exhibited only the characteristic peaks of anatase phase. After sulfation and calcination at 400 °C, nanotube structure had been transformed into anatase structure with lower symmetry according to the XRD results. Sodium titanate nanotube structure was not changed by impregnation of iron oxide, but the sulfation process induced phase transformation of sodium titanate into anatase.

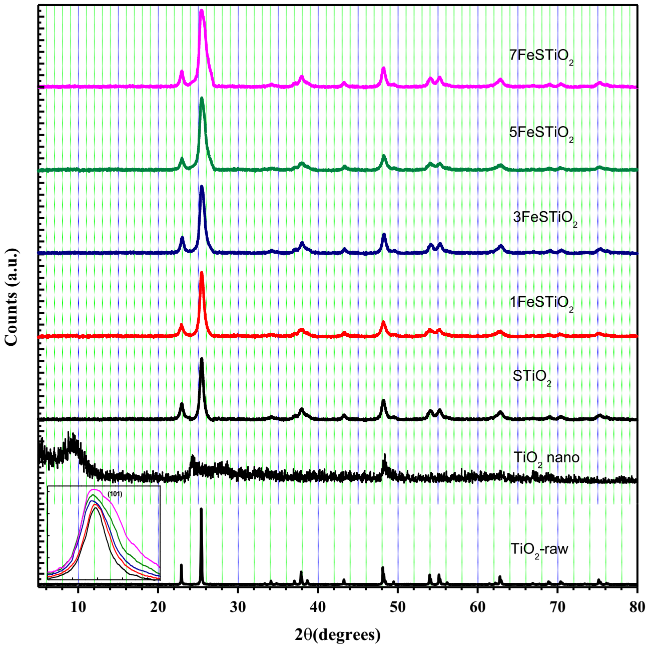

Fig. 1. Powder X-ray diffraction patterns of the samples.

The average crystallite size (Table 2) was calculated using Scherrer equation from the (101) reflection of anatase. It has been reported that the degree of crystallization of the sulfated oxides is much lower than that of the non-sulfated oxides [22]. It is noteworthy that the XRD patterns of the anatase phase became weaker and slightly wider (inset of Fig. 1) with the increase of iron loading. This finding suggests a decrease in the degree of crystallinity and the formation of smaller TiO_2 crystallites upon increasing the iron oxide loading. The absence of any diffraction lines of iron oxide phases, even at 7 wt% iron oxide loading, indicates that the iron oxide may be highly dispersed on the TiO_2 surface. It was reported that both Fe^{3+} (0.64 Å) and Ti^{4+} (0.68 Å) have similar ionic radius values, there is a possibility of $FeTiO_x$ solid solution formation within the crystal or at the interstices [23]. As iron oxide concentrations we used in the present study are relatively low, it is not possible to detect minor changes using XRD technique.

The EDX data (Table 1) shows the elemental composition of all the samples. Although the same concentration of sulfuric acid was utilized for sulfation of all the samples, their sulfate-retaining capacity was slightly different from each other. It is probably due to presence of the iron oxide which could stabilize the sulfate ions over layers on the surface of TiO_2 nano structure.

3.2. Raman spectroscopy

Raman spectroscopy is a frequently used technique to investigate the structural differences of TiO_2. Raman spectra of TiO_2 raw, TiO_2 nanotubes, 7 wt% iron oxide loaded sample before sulfation and 7 wt% iron oxide loaded sample after sulfation are shown in Fig. 2. The TiO_2 raw material showed peaks at 145, 200, 400, 520 and 640 cm^{-1}. It was reported that there are six Raman active modes for anatase at 144 cm^{-1} (E_g), 197 cm^{-1} (E_g), 399 cm^{-1} (B_{1g}), 513 cm^{-1} (A_{1g}), 519 cm^{-1} (B_{1g}) and 639 cm^{-1} (E_g). Rutile has total four Raman active modes that could be detected at 143 cm^{-1} (B_{1g}), 447 cm^{-1} (E_g), 612 cm^{-1} (A_{1g}) and 826 cm^{-1} (B_{2g}) [24]. The peaks appeared for TiO_2 raw sample are clearly matching with the Raman modes for anatase phase.

After hydrothermal treatment in presence of NaOH, the characteristic Raman peaks of anatase almost disappeared. New characteristic Raman peaks of sodium titanate were appeared. The peaks at 276 cm^{-1} and 910 cm^{-1} were assigned to the symmetric stretching mode of a short Ti–O bond of sodium titanate in layer structure [25]. The new peak appeared at 126 cm^{-1} can be assigned to Na–O bonds [25]. It

Table 2
Crystallite size of catalysts from XRD and TEM analyses.

Catalyst	Crystallite size (nm)	
	XRD	TEM
TiO_2-raw	51.7	–
TiO_2-nano	25.8	20.5
$STiO_2$	41.3	31.0
$1FeSTiO_2$	38.3	28.0
$3FeSTiO_2$	32.9	25.1
$5FeSTiO_2$	30.5	20.8
$7FeSTiO_2$	29.7	18.5

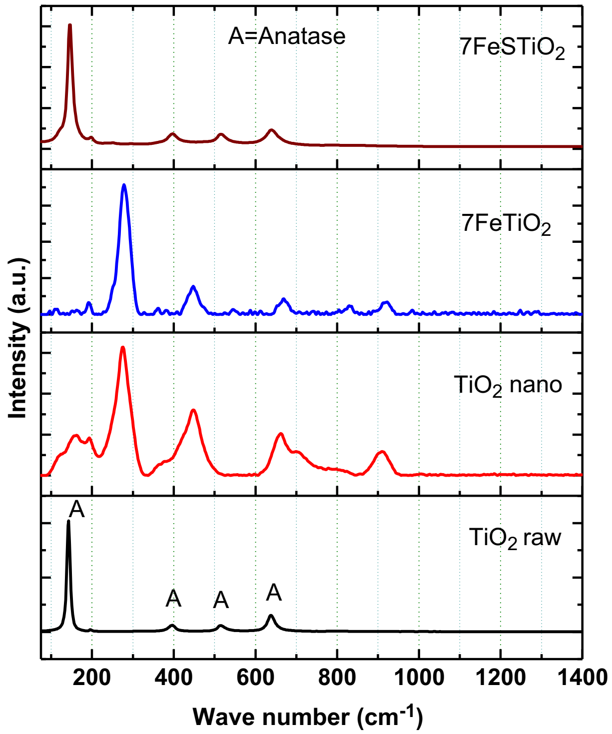

Fig. 2. Raman spectra of the selected samples.

Table 1
Textural and elemental composition data of catalysts.

Catalyst	BET surface area ($m^2\,g^{-1}$)	Micropore volume ($m^3\,g^{-1}$)	Mesopore volume ($m^3\,g^{-1}$)	Pore diameter (Å)	Elemental composition from EDX (%)		
					TiO_2	SO_4	Fe
TiO_2-raw	60	0.180	0.000	20	100	0.0	0.00
TiO_2-nano	254	1.716	0.054	200	100	0.0	0.00
$STiO_2$	202	1.174	0.055	100	90.7	9.3	0.00
$1FeSTiO_2$	182	1.024	0.154	100	90.08	9.0	0.92
$3FeSTiO_2$	130	0.613	0.267	34	88.26	8.8	2.94
$5FeSTiO_2$	125	0.591	0.363	54	86.41	8.7	4.89
$7FeSTiO_2$	98	0.210	0.421	38	85.00	8.1	6.90

is well known that sodium titanate with layer structure forms after treating TiO_2 with NaOH solution and it was considered to be the precursor of nanotubes. Another two peaks at 450 and 668 cm^{-1} could be attributed to Ti–O–Ti vibrations [26]. Sikhwivhilu et al. [21] have also observed similar Raman peaks for sodium titanate nanotubes in their study.

The nanotube sample with 7 wt% iron oxide before sulfation showed Raman peaks corresponding to TiO_2 structure with few changes in the spectrum. Washing with diluted HCl, impregnation with iron nitrate, and subsequent calcination of the sample at 400 °C brought few changes to the structure of the nanotubes. A broad peak centered at 162 cm^{-1} was disappeared. It is also interesting to note that the intensity and broadness of all the peaks were also decreased. Qian et al. [27] observed that two Raman peaks at 906 cm^{-1} and 126 cm^{-1} disappeared and a weak peak around 830 cm^{-1} appeared due to the covalent Ti–O–H bond after treatment of nanotubes with HCl. The authors also described that these changes are due to replacement of Ti–O–H bonds in place of Ti–O–Na bonds via ion exchange reaction during the catalyst preparation process.

The representative sulfated sample ($7FeSTiO_2$) showed Raman peaks corresponding to anatase phase. All the sulfated and iron oxide loaded samples showed same spectrum irrespective of amount of iron oxide loading, which indicates that anatase is the predominant species in all the samples. A similar observation was made by Sun et al. [28], they also observed that treatment of TiO_2 nanotubes with diluted sulfuric acid resulted in a change of the structure and morphology of the particles. Raman peaks corresponding to α-Fe_2O_3 appear at 225, 245, 292, 411, 498, 611, and 1323 cm^{-1}, and Fe_3O_4 exhibits a sharp band at 663 cm^{-1} [29]. However, the prepared iron oxide supported TiO_2 samples did not show the major bands of α-Fe_2O_3 (1323 cm^{-1}) and Fe_3O_4 (663 cm^{-1}). The Raman spectroscopy results indicated that there was no formation of crystalline iron oxides.

3.3. SEM and TEM analyses

Fig. 3 shows the SEM images of calcined TiO_2 raw (a), TiO_2 nanotube (b) and iron oxide loaded sulfated TiO_2 nanotubes samples. The surface morphologies of the samples are different from each other. The raw material comprised of granular crystalline particles with diameters of 50–100 nm. The structure of TiO_2 nanotubes was altered substantially from that of the raw TiO_2 material. The granular particles in the raw material had been transformed into nanotubes after NaOH treatment. The crystals exhibited a tube-like structure with a smooth surface and an outer diameter of around 8.4 nm; they were several hundreds of nanometers in length.

After sulfation and 1 wt% iron oxide loading [Fig. 3(c)], there was no change in the morphology of the titanate nanotubes. However, the increase of iron oxide loading to 3 wt% changed the morphology of nanotubes to the nanorods, and the formed nanorods aggregate together in irregular fashion. It is interesting to note that $3FeSTiO_2$ [Fig. 3(d)], $5FeSTiO_2$ [Fig. 3(e)], $7FeSTiO_2$ [Fig. 3(f)] samples consisted of dense TiO_2 nanorods.

Fig. 4 shows TEM images of calcined TiO_2 nano (a), $STiO_2$ (b) and iron oxide loaded $STiO_2$ samples. Hollow, open-ended and randomly tangled TiO_2 nanotubes were obtained after NaOH treatment. The TiO_2 nanotubes were measured to be about 5–8 nm in diameter, with about 1 nm wall thickness, and the lengths in the range of 50–200 nm. In the $1FeSTiO_2$ sample [Fig. 4(c)], the formation of tubular structure was clearly observed. With the increase of iron oxide loading to 3 wt% [Fig. 4(d)], there was a formation of dense structure of coagulated nanorods. The diameters of the nanorods were nearly uniform with lengths of approximately 60–100 nm. The nanorod structures had outer diameters of approximately 45 nm. With further increase of iron oxide loading to 5 wt% [Fig. 4(d)] and 7 wt% [Fig. 4(e)], formation of more coagulated dense particles can be observed. The compaction of the particle aggregates suggests that the nanotubes have transformed into nanorods or nanoparticles after iron oxide loading. These observations are in quite accordance with SEM results. It appears that the dispersion of iron oxide nanoparticles is varying with change in its loading. The sample contained 7 wt% iron oxide loading showed poor iron oxide dispersion due to severe coagulation of the particles.

The average diameter of TiO_2 nanorods is about 50 nm for $1FeSTiO_2$ and $3FeSTiO_2$ samples. Samples with high iron oxide (5 wt% and 7 wt%) loading formed relatively more and bigger bundled nanorod structures. This implies that $7FeSTiO_2$ and $5FeSTiO_2$ samples are more agglomerated than $3FeSTiO_2$ and could be ascribed to the difference in the surface charges, the presence of more iron ions on the surface of $5FeSTiO_2$ and $7FeSTiO_2$ samples could lead to increased surface charge and electrostatic attraction of individual nanorods subsequently leading to the pronounced agglomeration of particles. The results from XPS analysis of the samples which were presented in the later section are supporting this observation.

The HRTEM images of TiO_2 nano and $7FeSTiO_2$ samples are shown in Fig. 4(f) and (g) respectively. The images are indicating that the prepared nanotubes had uniform inner (ca. 4.5 nm) and outer diameters (ca. 9 nm) along the length. Moreover, they possessed multi-walled tubular structures and generally consisted of 2–4 layers, also as presented in Fig. 4(f). The interlayer distance, directly measured from HRTEM image, was ca. 0.75 nm.

3.4. N_2 adsorption–desorption

Fig. 5 shows nitrogen adsorption–desorption isotherms and corresponding pore size distribution patterns (inset) of all the samples. All the samples have isotherms of type IV and hysteresis loops of type H_3 at relative pressure range of 0.8–1.0. According to the IUPAC classification, the type H_3 is associated to aggregates or agglomerates of particles with non-uniform size and/or shape which could contribute to formation of inter-particle mesopores. Moreover, the observed hysteresis loop approaches $P/P^0 = 1$ in case of TiO_2 nano sample, suggesting the presence of macropores in this sample. The BJH pore size distributions of the samples are shown in the inset of the figure; the as-prepared titanate nanotubes have only one kind of large pores. Considering the morphology of the

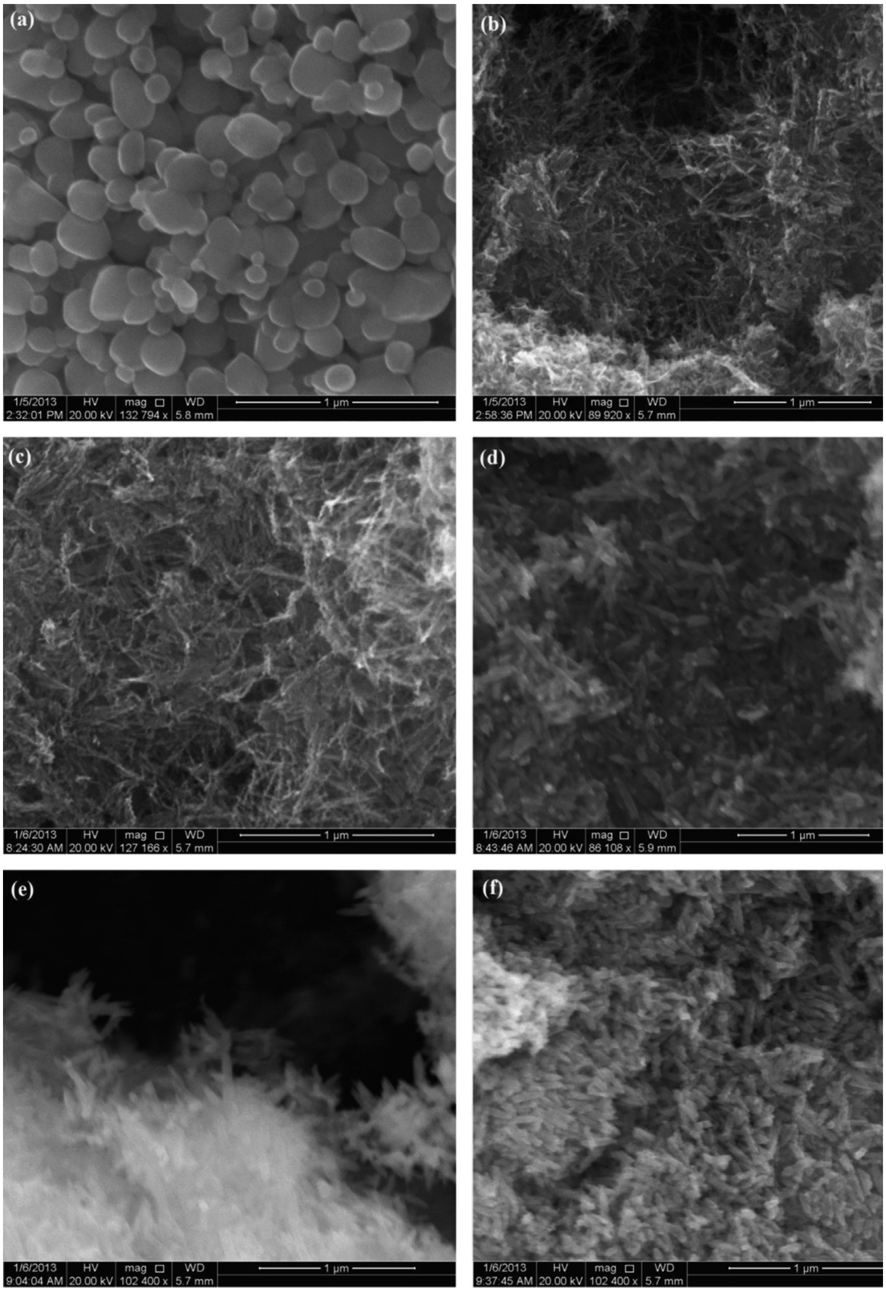

Fig. 3. SEM images of (a) TiO_2-raw, (b) TiO_2 nano, (c) 1FeSTiO_2, (d) 3FeSTiO_2, (e) 5FeSTiO_2 and (f) 7FeSTiO_2.

nanotubes observed in SEM and TEM analyses, the pores with large size (200 Å) may ascribe to the aggregation of the nanotubes. The larger pores were probably due to the interior space of the nanotubes while the smaller pores could be associated with the interstice crystalline walls of the TiO_2 nanorods. After sulfation and 1 wt% iron oxide impregnation, the pore size is decreased to 100 Å. With further increase of iron oxide loading from 3 to 7 wt%, the larger pores were disappeared and appearance of pores with small size were observed.

Textural parameters determined from N_2-physisorption experiments are presented in Table 1. When the raw TiO_2 powder transformed into the TiO_2 nanotubes, there was a significant increase in specific BET surface area from 60 to 254 $m^2\,g^{-1}$ and for total pore volume from 0.18 to 1.77 $cm^3\,g^{-1}$, respectively. The total pore volume of the TiO_2 nano, STiO_2 nano, 1FeSTiO_2, 3FeSTiO_2, 5FeSTiO_2, and 7FeSTiO_2 were determined to be 1.178, 0.880, 0.954 and 0.631 $cm^3\,g^{-1}$, respectively (Table 1). As also shown in Table 1, the sample had relatively large surface areas for 1FeSTiO_2 sample. The surface area, the mesopore volume and the average pore diameter decreased with increasing iron oxide loading. The small specific surface area can be attributed to the destruction of nanotubular structure. From the TEM analysis it is clear that the aggregation of nanorods resulted in closely packed coagulated structure which is probably responsible for low extent of exposition to N_2. Although, the surface area and mesopore volume decreased after iron oxide loading, the

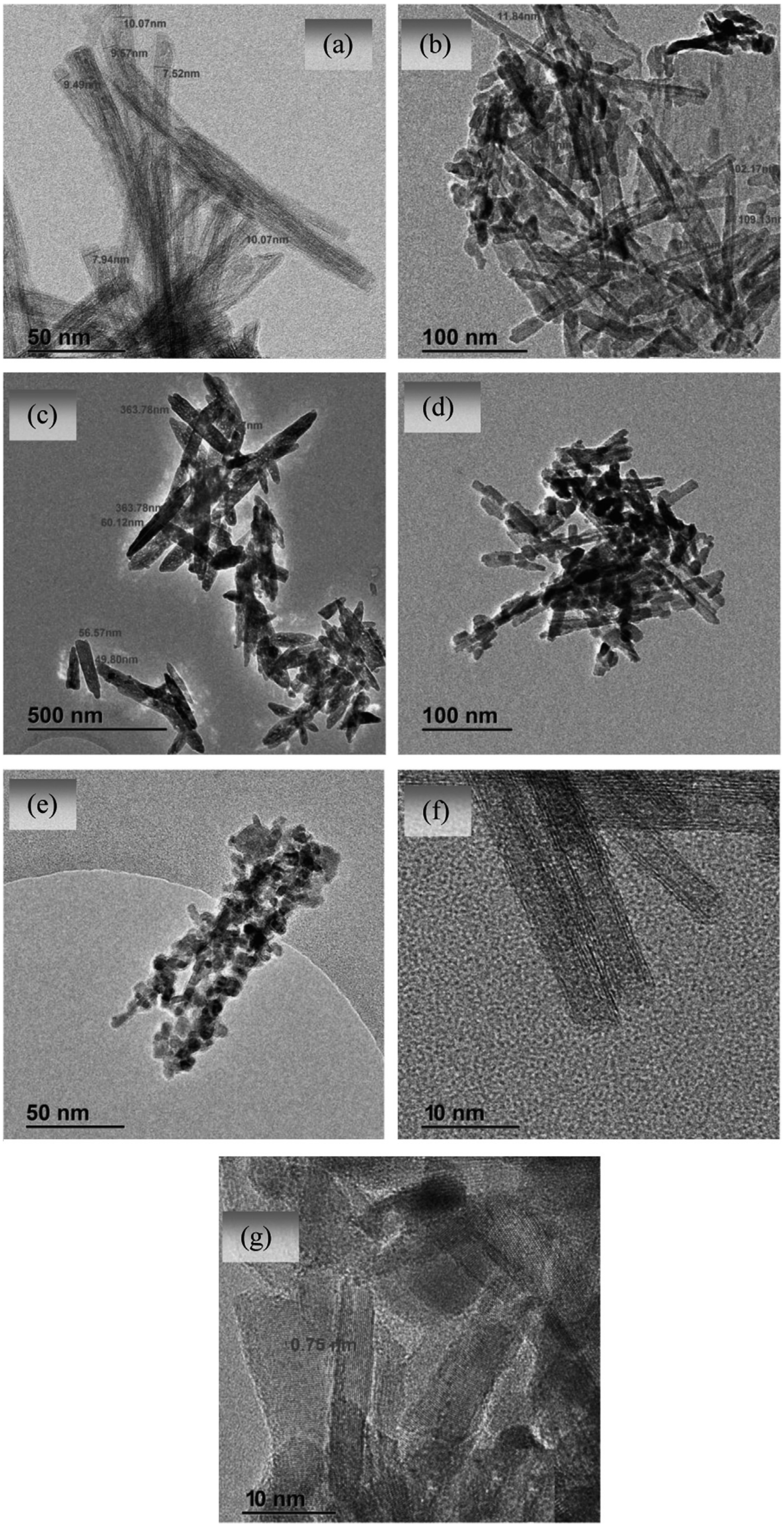

Fig. 4. TEM images of (a) TiO_2 nano, (b) $1FeSTiO_2$, (c) $3FeSTiO_2$, (d) $5FeSTiO_2$, (e) $7FeSTiO_2$, (f) HRTEM image of TiO_2 nano and (g) HRTEM image of $7FeSTiO_2$.

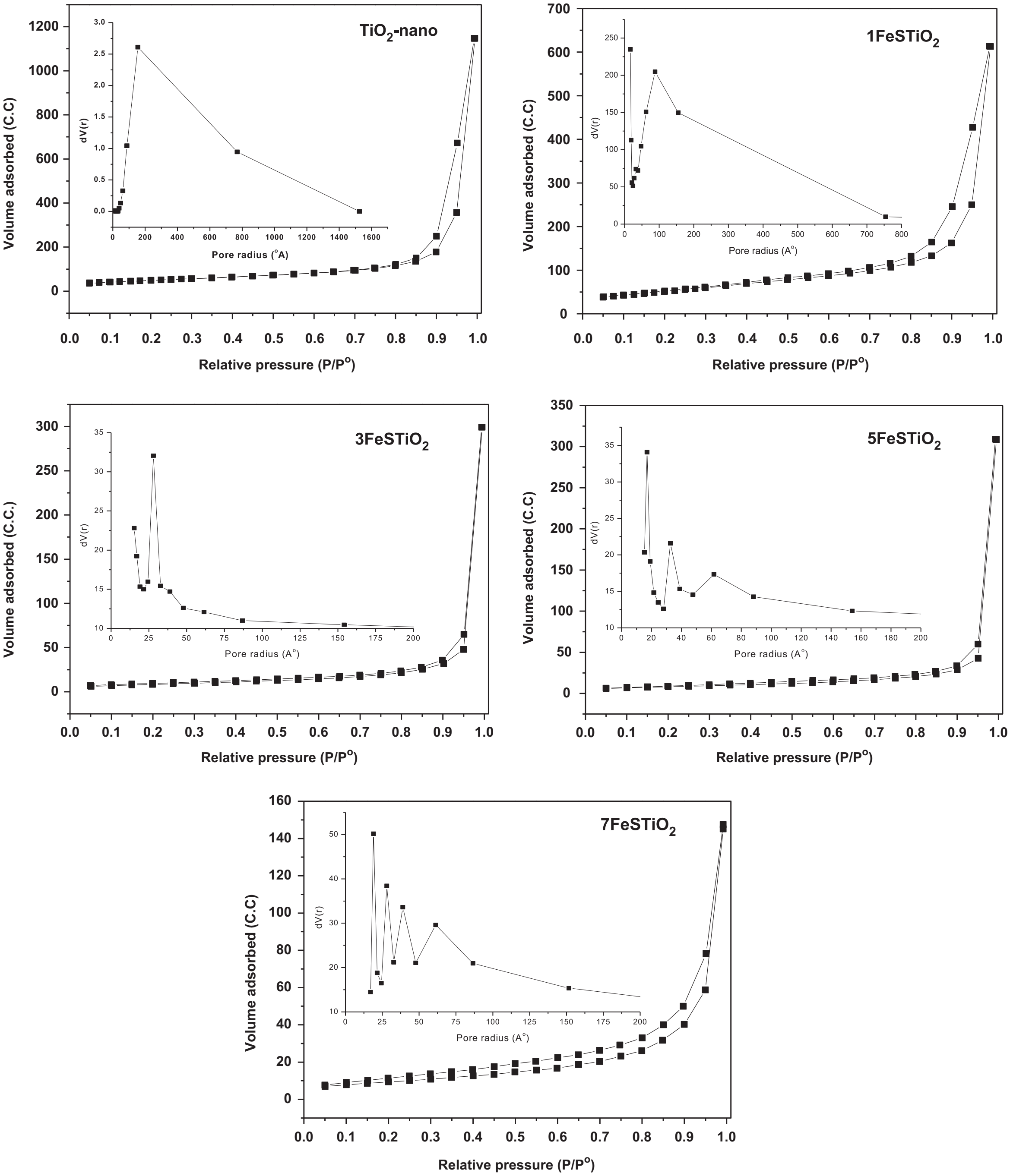

Fig. 5. N_2 gas adsorption–desorption isotherms (inset pore size distribution) of samples.

xFeSTiO$_2$ samples still possess much higher surface area and pore volume than TiO$_2$ raw powder.

3.5. X-ray photoelectron spectroscopy (XPS)

The catalysts were further analyzed by XPS to identify the surface nature and atomic concentration of various elements. Fig. 6 (a) shows the Ti 2p XPS spectra of the TiO$_2$ nano, 1FeSTiO$_2$, 3FeSTiO$_2$, 5FeSTiO$_2$, and 7FeSTiO$_2$ samples. Two signals can be observed with two components, first at 458.5 eV for the Ti 2$p_{3/2}$ and second at 464.1 eV for the Ti 2$p_{1/2}$, corresponding to the Ti 2p spin-orbit components of Ti(IV) surface species. In comparison with TiO$_2$ nano sample, the xFeSTiO$_2$ samples show a shift of Ti 2$p_{3/2}$ binding energies of 1.1 eV. Hou et al. [30] also observed a shift to higher binding energy (0.5 eV) in case of sulfated TiO$_2$ samples and the authors attributed the shift to increase in effective positive charge around Ti(IV) surface species, which is due to strong interaction between the sulfate anion and Ti cation. Sohn et al. [31] also reported a similar observation and revealed that such interaction was a driving force in the generation of a large amount of surface acidic sites on the surface of sulfated metal oxides. The iron oxide loading has no effect on the Ti 2p peak, indicating that

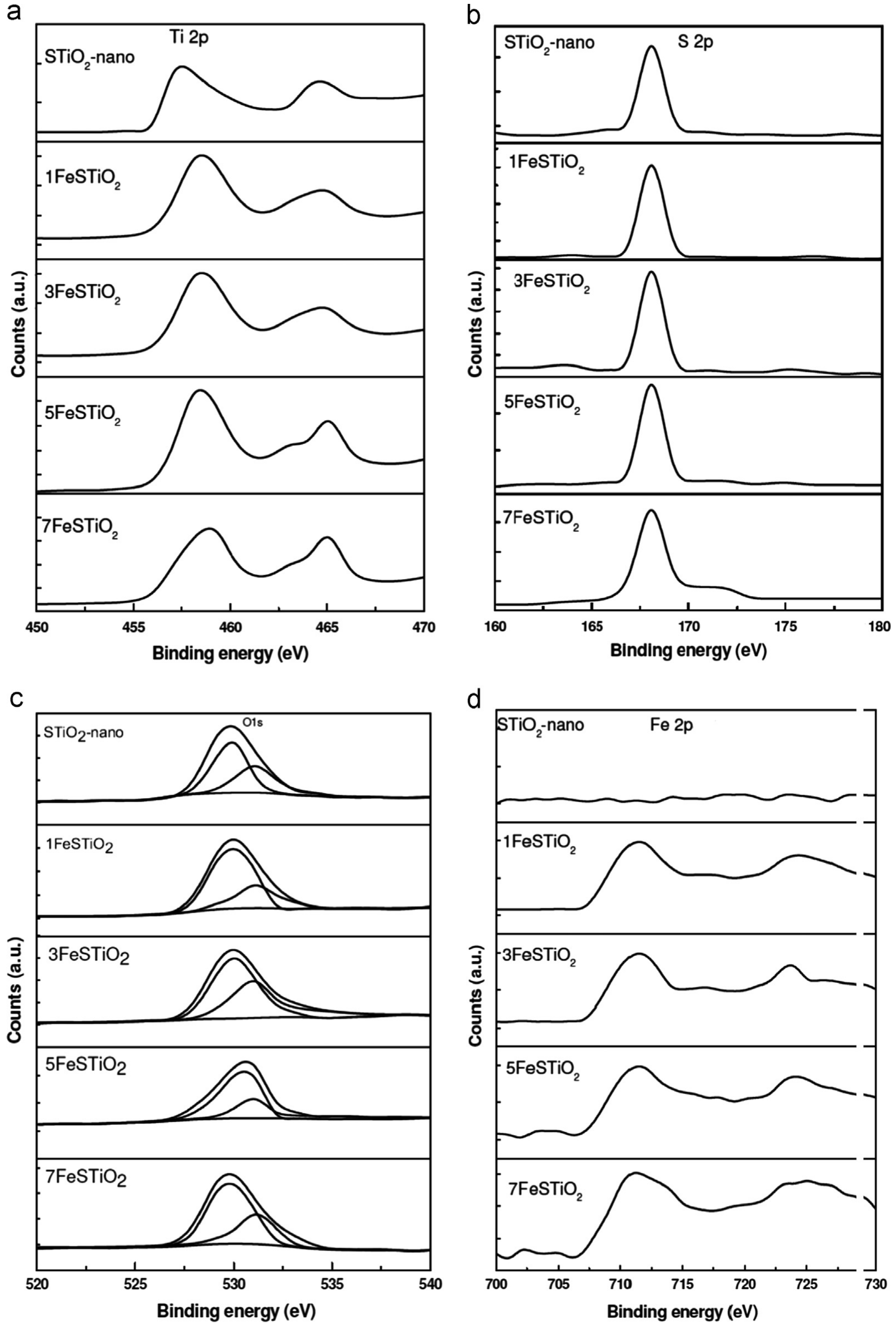

Fig. 6. XPS spectra of samples: (a) Ti 2*p*, (b) S 2*p*, (c) O 1*s* and (d) Fe 2*p*.

iron oxide loading did not changed the coordination and chemical state of Ti^{4+} ions.

The S 2*p* XPS spectra of all the samples are shown in Fig. 6 (b). All the spectra display a single dominant peak at 168 eV which was assigned to the sulfate species [30]. Addition of iron oxide had no effect on the binding energy of the signal and also with increase of the iron oxide loading; there was no significant change in the signal intensity.

Fig. 6(c) shows the O 1*s* spectra of the samples. The O 1*s* spectrum of TiO_2 nano consists of two peaks. A major peak appears at 530 eV with a small shoulder peak centered at 532 eV. The main peak could be assigned to Ti–O in TiO_2, and the other minor peak is due to O–H on the surface of TiO_2 [32]. In the case of the sulfated samples, the signals can be fitted by three curves in between 531 and 532 eV, which can be attributed to Ti–O (530 eV), S–O (530.8 eV) and O–H (531.7 eV) components, respectively [33].

The Fe 2*p* core-level spectra of the catalysts are shown in Fig. 6(d). All the iron oxide containing samples showed peaks corresponding to the two levels, Fe $2p_{3/2}$ and Fe $2p_{1/2}$, and also the satellite peak. The peak appeared at 711 eV can be ascribed to Fe^{3+} ions. This is an expected result because we used Fe $(NO_3)_3$ as iron source, thus, the Fe element in the samples exists mainly in the +3 oxidation state. It can be observed that the chemical binding energy at 711.3 eV of Fe^{3+} is different from that of Fe^{3+} in Fe_2O_3 (at 710.9 eV) [34]. It was reported that variations in the binding energies (0.4 eV) arise from the difference in the chemical potential and polarizability of $FeSTiO_2$ nanorods and Fe_2O_3 [23]. The atomic concentration of each element was obtained by peak area integral of its spectrum. All the samples showed more surface iron content than the nominal composition, suggesting that the iron had a much higher concentration at the surface than in the bulk of the TiO_2. These observations are indicating that there was a strong interaction between Fe^{3+} and SO_4^{2-} ions, which allowed forming an isolated interactive species on the TiO_2 surface [35]. It is possible for the Fe ions to enter into TiO_2 bulk beside surface, since the carrier excitation Bohr radius in TiO_2 is only ca. 2 nm [36]. However, it is known that the amount of iron oxide doped into the TiO_2 bulk is dependent on the particle size of the TiO_2 support [37]. More Fe ions can enter into the bulk of larger TiO_2 particles. In this case, Fe ions are mainly on surface due to the small particle size of TiO_2, which can form effective species for redox reactions.

3.6. H_2-temperature programmed reduction (H_2-TPR)

H_2-TPR profiles of $STiO_2$ nano and other $FeSTiO_2$ samples are shown in Fig. 7. It can be observed that sulfated TiO_2 sample without iron oxide loading did not show any clear reduction peak below 550 °C, but the iron oxide loaded samples showed clear reduction peaks. The reduction of iron oxides took place in the temperature range 225–450 °C. Klose et al. [38] previously observed a promotion effect of iron on the reducibility of sulfated zirconia support that presence of sulfate species lead to decrease the reduction temperature of the catalysts. The $1FeSTiO_2$ sample exhibited major peak with temperature maximum placed approximately at 280 °C. This peak can be assigned to simultaneous reduction of sulfate and iron species [39]. With increase of iron oxide loading to 3 wt %, 5 wt% and 7 wt%, the reduction peak became broad and overlapped with four different sub-peaks. We used peak fitting software to deconvolute the peaks for all the samples. Liu et al. [40] also observed overlapped reduction peaks for iron titanate samples. They performed the deconvolution of the broad peak and concluded that it consists of four sub-peaks which could be ascribed to the progressive degrees of Fe^{3+} reduction, but not the reduction of Fe^{3+} species in different dispersive states. The four sub-peaks can be attributed to the reduction of surface adsorbed oxygen, lattice oxygen from Fe^{3+}–O–Ti, lattice oxygen from $Fe^{2+/3+}$–O–Ti at surface and inner layers, respectively.

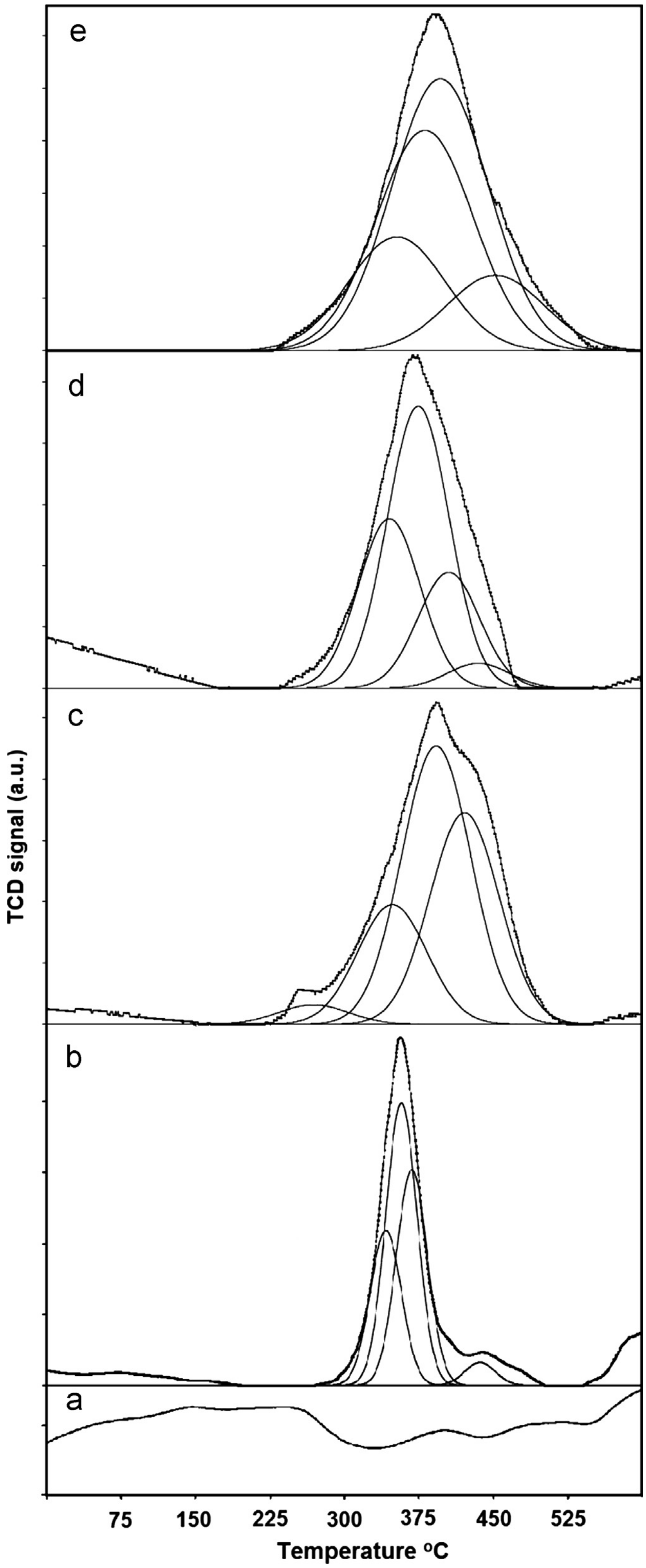

Fig. 7. H_2-temperature programmed reduction patterns of (a) TiO_2 nano, (b) $1FeSTiO_2$, (c) $3FeSTiO_2$, (d) $5FeSTiO_2$ and (e) $7FeSTiO_2$.

The extent of reduction of the samples was calculated as the H_2 consumption per mole of Fe_2O_3 and the values are tabulated in Table 2. For all the samples, the extent of H_2 consumption is higher than the value of 1.0 expected for stoichiometric reduction of Fe_2O_3 to 2FeO. This enhancement in H_2 consumption is possibly due to the removal of sulfate ions by reduction. It can also observe that $1FeSTiO_2$ (1.03), $3FeSTiO_2$ (1.05) and $5FeSTiO_2$ (1.10) samples showed comparable H_2 consumptions per one mole of Fe_2O_3, which are close to the stoichiometric requirement. However, $7FeSTiO_2$ (1.58) sample displayed high value of H_2 consumption than the stoichiometric value, suggesting that a slight reduction to Fe^0 took place in this sample. It is known that the bulk Fe_2O_3 could be only reduced to Fe_3O_4 beyond 500 °C [40]. The H_2-TPR results indicating that the iron species in $FeSTiO_2$ samples were totally reduced from Fe^{3+} to Fe^{2+} below 500 °C. It is interesting to note that the reduction peak of $5FeSTiO_2$ catalyst was shifted to lower temperature than other samples indicating that $5FeSTiO_2$ sample is easily reducible than the other samples. The extent and easy reducibility of $FeSTiO_2$ samples is an indication that these materials possessed higher mobility of lattice oxygen, which could be beneficial to enhance the oxidative ability and thus the SCR activity.

3.7. Pyridine adsorption using FTIR technique

Adsorption of pyridine (as probe molecule) on the catalyst surface is widely used to characterize the surface acidity of the catalysts. The adsorbed pyridine could be easily analyzed by FTIR spectroscopy to distinguish the different acid sites presented in the samples [41]. FTIR pyridine adsorption spectra of the all the samples are shown in Fig. 8. As shown in the figure, all the spectra showed additional peaks at 1447, 1489 and 1540 cm^{-1}. These peaks were appeared due to the chemisorption of pyridine molecules on different type of surface acidic sites [42]. The peak at 1447 cm^{-1} was due to the interaction of pyridine with Lewis acidic sites (exposed metal cations), while the peak at 1540 cm^{-1} was due to the protonation of pyridine molecule by the Brönsted acid sites (surface-bound sulfate groups) [43]. The peak at 1489 cm^{-1} was due to the vibration of pyridine adsorbed on both Brönsted acidic sites (B) and on Lewis acidic sites (L) [43]. These results are indicating that the sulfated TiO_2 and iron oxide supported $STiO_2$ samples possessed both Lewis and Brönsted acid sites.

It should be noted that only small peaks corresponding to pyridine adsorbed on Lewis acidic sites were observed for TiO_2 nano sample. This observation suggested that the surface acidity of TiO_2 nano sample was too weak to react with pyridine molecules at room temperature. Therefore, sulfate modification not only increased the number of strong Lewis acidic sites, but also induced a large amount of Brönsted acidic sites on the surface of TiO_2. It is known that strong Brönsted and Lewis acidic sites could provide better adsorption centers for NO_x molecules. With the increase of iron oxide loading from 1 wt% to 7 wt%, the intensity of the peak at 1447 cm^{-1} (Lewis acid sites) was increased and the intensity of the peak at 1540 cm^{-1} (Brönsted acid sites) was slightly decreased, suggesting that iron oxide loading had an influence on the acid sites of the catalyst. This is possibly due to presence of S=O covalent bonds, which can act as an electron withdrawing species, leading to stronger Lewis acid strength of Fe^{3+} [44].

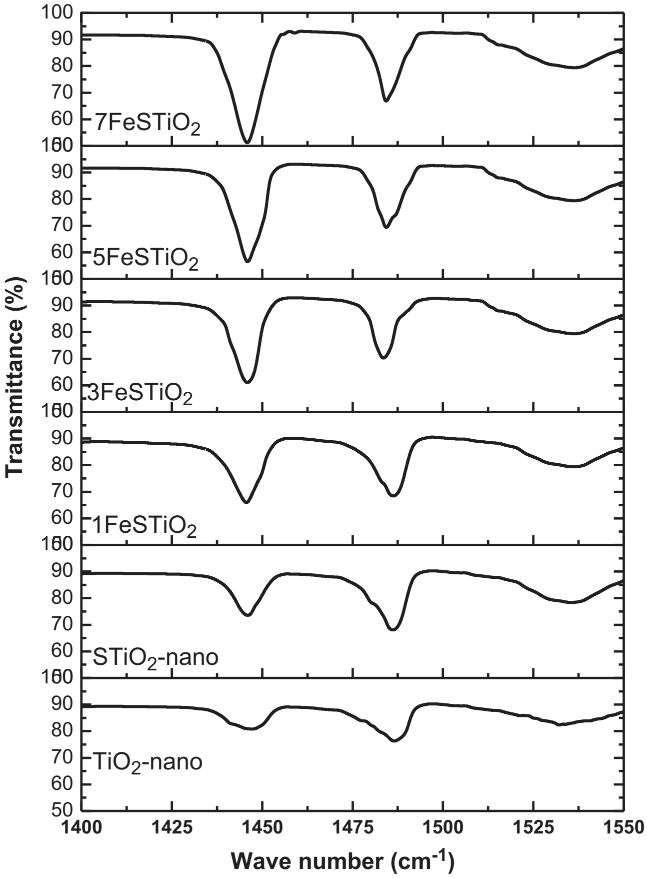

Fig. 8. FTIR spectra of pyridine adsorbed samples.

Chmielarz et al. [45] previously reported that the deposition of iron or copper by the ion exchange method resulted in a decrease in the concentration of Brönsted acidic sites and an increase in the number of Lewis acidic sites. The concentration of Brönsted and Lewis acid sites on the samples was obtained by integrating the area of peaks at 1542 and 1447 cm^{-1}, respectively. Values of concentration of Brönsted and Lewis acid sites after pyridine chemisorption are presented in Table 3. With the increase of iron oxide loading from 1 wt% to 7 wt%, the B/L ratio increased slightly from 0.82 to 2.1. These results clearly indicated that the impregnation of iron oxide led to an increase of number of Brönsted and Lewis acidic sites of the samples.

3.8. Selective reduction of NO with propane

It is known that the presence of oxygen is essential to NO reduction. Therefore, there are two reaction pathways for the propane oxidation which could be represented as

$$C_3H_8+2NO+4O_2 \rightarrow N_2+3CO_2+4H_2O \quad (2)$$

$$C_3H_8+5O_2 \rightarrow 3CO_2+4H_2O \quad (3)$$

Table 3
FTIR-pyridine adsorption and XPS data of the catalysts.

Catalyst	**Brönsted acid sites (*B*)**	**Lewis acid sites (*L*)**	***B*/*L* ratio**	**Atomic concentration from XPS (%)**			
				O 1*s*	**Ti 2*p***	**Fe 2*p***	**S 2*p***
$STiO_2$	456	216	2.10	69.14	25.2	0.00	5.66
$1FeSTiO_2$	407	278	1.46	69.97	23.0	1.42	5.61
$3FeSTiO_2$	359	325	1.10	71.35	19.2	3.74	5.71
$5FeSTiO_2$	340	350	0.97	72.46	16.5	5.29	5.75
$7FeSTiO_2$	294	421	0.69	72.92	13.8	7.50	5.78

The SCR of NO activity of all the catalysts was tested using steady-state reaction conditions. Under our experimental conditions, the products of the reaction were N_2, NO_2 and CO_2. Formation of CO was not observed in the studied temperature range (300–500 °C).

Fig. 9(a) shows the NO conversions as a function of reaction temperature over a series of xFeSTiO$_2$ nanotube catalysts with different iron oxide contents. It can be seen that TiO_2 nano and $STiO_2$ samples were slightly active for the SCR of NO with propane. In contrast, the catalytic activities of $STiO_2$ were remarkably enhanced after the catalysts loaded with 1 wt%, 3 wt%, 5 wt% and 7 wt% of iron oxide. Especially for the 5 wt % iron oxide supported $STiO_2$, over which the maximum NO conversion reached to 90% at 450 °C. The variation of the NO conversion as a function of the reaction temperature shows that conversion increased with temperature up to 450 °C and then decreased with further increase to 500 °C.

It is clear that with increasing of iron oxide content from 1 wt% to 5 wt%, the conversion of NO was increased at all the studied reaction temperatures and further increase of loading to 7 wt% led to decrease of NO conversion. This result indicates that there exists an optimum content for iron oxide. The maximum NO conversions as a function of the catalysts followed the order: $5FeSTiO_2 > 7FeSTiO_2 > 3FeSTiO_2 > 1FeSTiO_2$. On the other hand, it can be observed from Fig. 9(b) that the conversion of propane increased with the iron oxide content, indicating that the iron oxide loaded on $STiO_2$ nanotube catalyst has an effect on activating propane. As shown in Fig. 9, the optimum iron oxide content of $FeSTiO_2$ is about 5 wt%. Therefore, the $5FeSTiO_2$ was chosen to conduct further investigations.

In order to elucidate the effect of sulfation on the catalytic performance of the catalysts, we compared the NO and propane conversions at 400 °C over TiO_2 nano, $STiO_2$ nano, $5FeTiO_2$, and $5FeSTiO_2$, and the results are shown in Fig. 10 (a). It can be seen that both TiO_2 nano and $STiO_2$ nano were only slightly active for the SCR of NO with propane. However, after loading them with iron oxide, the results were completely different for TiO_2 nano and $STiO_2$ nano catalysts. The $5FeTiO_2$ catalyst was less active than TiO_2 nano for the SCR of NO with propane, while the conversion of propane over the $5FeTiO_2$ was much higher than that over TiO_2 nano. On the contrary, when the TiO_2 nanotubes support was sulfated, the NO conversion over the $5FeSTiO_2$ was significantly higher than that over $STiO_2$. To further clarify the role of sulfation on the catalytic performance of $FeTiO_2$ nanotube catalysts, the conversions of propane on the $5FeTiO_2$ and the $5FeSTiO_2$ in the unit reaction of propane–oxygen were compared. As shown in Fig. 10(b), it was clear that the conversion of propane over the $5FeTiO_2$ in the unit reaction of propane–oxygen was higher than that over the $5FeSTiO_2$ under the same conditions, indicating that the sulfation of the TiO_2

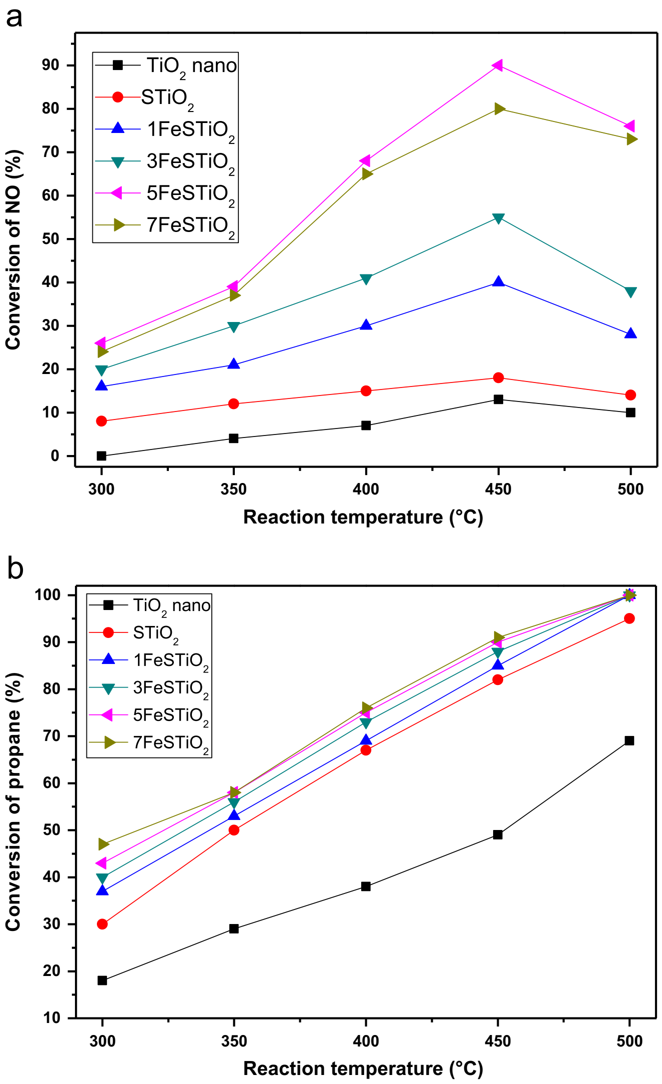

Fig. 9. SCR of NO activity of catalysts at different reaction temperatures: (a) conversion of NO and (b) conversion of propane.

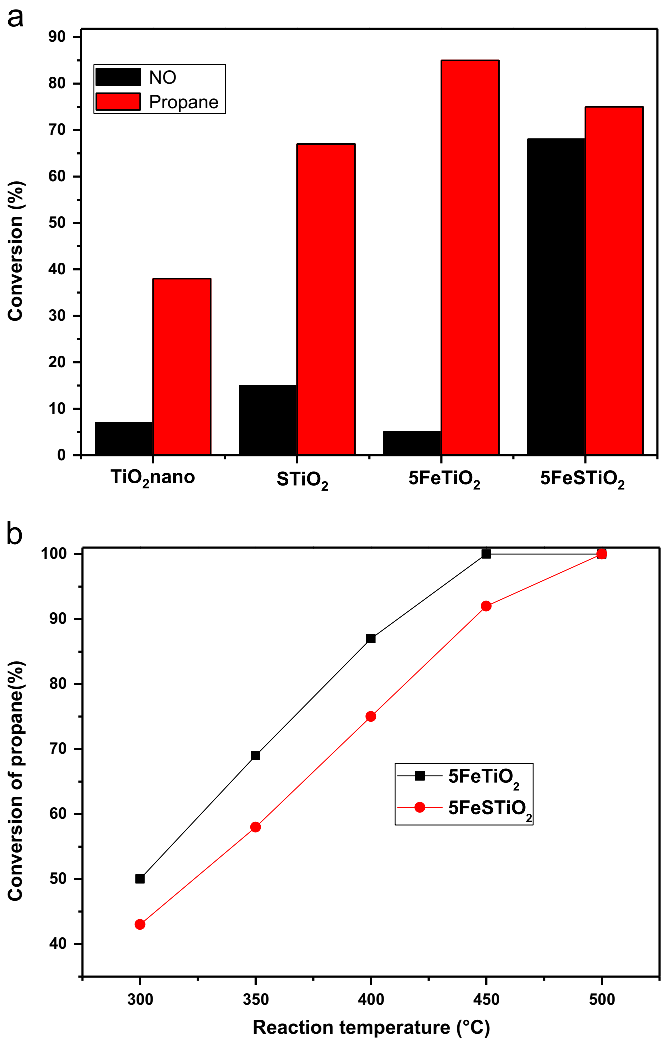

Fig. 10. Effect of sulfation of catalysts: (a) comparison of SCR of NO activity between TiO_2 nano, $STiO_2$, $FeTiO_2$ and $FeSTiO_2$, and (b) propane–oxygen unit reaction activity of $5FeTiO_2$ and $5FeSTiO_2$ catalysts.

nanotube material led to suppression of combustion reaction of propane.

It was reported that the adsorption of oxygen can occur at the vacancy sites of TiO_2 [46]. The adsorption of propane data on TiO_2 and on iron species dispersed on TiO_2 in the temperature range of 300–500 °C is not studied in the present work. However, opposite to the poor oxidation activity of pure TiO_2, the $STiO_2$ and iron oxide supported $STiO_2$ samples exhibited very high oxidation activity. Therefore, the existence of nano-sized iron oxide species along with the presence of sulfate groups leads to the difference in the propane adsorption and catalytic reaction of the iron oxide supported sulfated TiO_2 samples.

The characterization data (XRD and Raman) showed that the sulfation process efficiently dispersed the iron oxide species of the $FeSTiO_2$ catalysts and prevented the formation of bulk oxide thus suppressed the combustion reaction of propane and increased the selectivity of propane towards NO reduction. However, the increase of iron oxide loading above 5 wt% leads to decrease of NO conversion. The pronounced decrease in catalytic activity of $7FeSTiO_2$ catalyst could be related to formation of coagulated iron oxide particles on the surface of the TiO_2 support (TEM results). On the other hand, the sulfation of the TiO_2 nanotubes greatly increased the acid sites of the catalysts, which is essential for the SCR of NO with propane [14].

It was also observed in XPS results that after sulfation, both of the Fe 2*p* and Ti 2*p* bands shifted towards higher binding energies. This was mainly due to the inductive effect of the S$=$O covalent double bond with a much stronger affinity to electrons [47] implying an enhanced Lewis acid strength of metallic sites on the catalyst surface [48] Therefore, together with the Brönsted acid sites introduced by sulfate species itself, and Lewis acid strength derived from metallic sites on $FeTiO_2$ catalysts were also simultaneously improved by the sulfation process. These acid sites could enhance the adsorption of propane, supplying more reducing agent for the SCR reaction.

The type of acidic site was one of the important features influencing catalytic performance. An attempt was made to draw a correlation between iron oxide loading and *B*/*L* ratio and its subsequent effect on the conversion of NO (Fig. 11). It is clear that iron oxide loading have great influence on the acidity nature and conversion of NO. Jung and Grange investigated the reaction intermediate during NO reduction over a sulfated TiO_2 [14]. The authors concluded that the reaction rate of NO removal on sulfated TiO_2 catalyst depended on the amount of Lewis acid sites presented on the catalyst surface. Lewis acid sites dominated in all $FeSTiO_2$ samples, which were found to be active catalysts for the SCR of NO_x process. In the present case, it appears that maximum conversion can be obtained with the catalyst which possessed *B*/*L* ratio around 1.0.

Kikuchi and Yogo [49] proposed that NO is oxidized to NO_2 on Brönsted acid sites followed by their migration to an active metal site where a direct NO_2-hydrocarbon reaction would take place. In this route, the Brönsted sites indirectly participate in the C–H bond cleavage by oxidizing NO to form the reactive species, NO_2. Upon the formation of NO_2, a reaction proceeds involving adsorbed propane species. In this step the migration of NO_2 cannot be excluded. In another

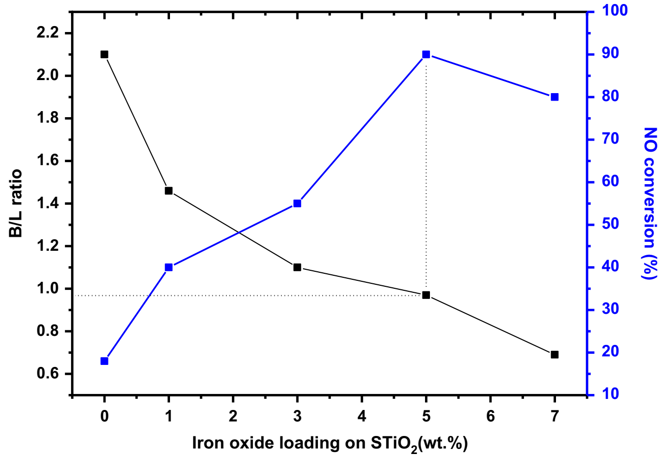

Fig. 11. Correlation among iron oxide loading, *B*/*L* ratio and NO conversion.

report, Kantcheva and Vakkasoglu [50] studied the reaction mechanism using FTIR technique for the SCR of NO with methane over cobalt supported sulfated zirconia catalyst. The authors suggested that methane was partially oxidized to formate or formic acid species over strong Lewis acid sites. They also suggested that formate or formic acid species are more active and can selectively reduce nitric oxides to nitrogen.

Here, we propose a similar pathway [Eqs. (4) and (5)] to that of Kantcheva and Vakkasoglu [50]. From the characterization and catalytic activity results, we suggest that the reduction of NO by propane on these Fe-containing catalysts most probably takes place according to the following steps:

Oxidation of NO to NO_2 in presence of oxygen over the iron sites, which possessed high mobile oxygen capability.

$$NO + 1/2O_2 \rightarrow NO_2 \text{ [metal sites]} \quad (4)$$

Protonation of propane on strong Brönsted and Lewis acid sites of metal-sulfate species to form $C_3H_9^+$, which decomposes into H_2 and $C_3H_7^+$ or methane and $C_2H_5^+$.

$$2NO_2 + C_3H_8 + 3O_2 \rightarrow N_2 + 3CO_2 + 4H_2O \text{ [metal-sulfate sites]} \quad (5)$$

It was reported that addition of iron or manganese to sulfated zirconia promotes redox process, which accelerates the protonation of alkanes to form carbenium ions and kicks off the conventional catalytic cycles [51].

Therefore, it is clear that strong surface acidity and high oxidation ability of the $FeSTiO_2$ catalysts due to presence of iron oxide and sulfated species are favoring high SCR activity. This argument is supported by reaction product analyses using FTIR and catalytic tests that display the conversion of NO and propane began simultaneously.

To check the stability of iron oxide supported TiO_2 nanotube catalysts, a long term on-stream activity test was carried out over the highly active (i.e. $5FeSTiO_2$) catalyst. From the results shown in Fig. 12, no deactivation was observed during the 50 h test, which indicated that these catalysts have good stability.

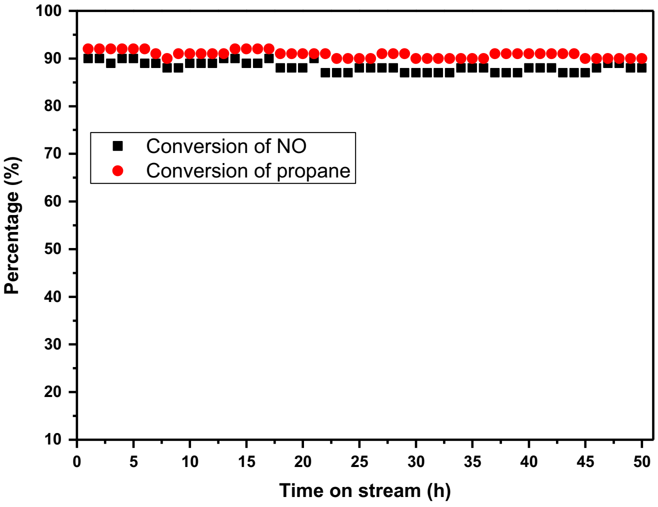

Fig. 12. Time on stream analysis of $5FeSTiO_2$ catalyst.

4. Conclusions

A series of iron oxide loaded sulfated TiO_2 nanotube catalysts were used for the first time for the SCR of NO with propane. Catalytic activity results demonstrated that these catalysts are efficient in the SCR of NO with propane in particular 5 wt% iron oxide loaded sulfated TiO_2, which offered 90% of NO conversion at 450 °C. Both the iron oxide loading and the sulfation of the TiO_2 nanotube played an important role in determining the catalytic performances. The results of XRD, N_2-adsorption, XPS, H_2-TPR, FTIR spectra of pyridine adsorption indicate that the addition of iron to the sulfated TiO_2 catalyst increased the surface area of sulfated TiO_2 and the amount of strong Brönsted acid sites (active center for the SCR of NO) and Lewis acid sites (the activation of propane) on sulfated TiO_2. Moreover, sulfation process also helped the dispersion of the easily reducible isolated Fe^{3+} species. As the result, the $x$$FeSTiO_2$ catalysts were more active for the SCR of NO with propane. Long term measurements over 50 h indicated a very good stability of these catalysts for SCR of NO.

Acknowledgments

This work was funded by the Deanship of Scientific Research (DSR), King Abdulaziz University, Jeddah, under Grant no. (130-020-D1433). The authors, therefore, acknowledge with thanks DSR technical and financial support. Authors also thank Professor Suprakas Sinha Ray for his help in TEM analysis.

References

[1] M.V. Twigg, Progress and future challenges in controlling automotive exhaust gas emissions, Applied Catalysis B: Environmental 70 (2007) 2–15.

[2] M. Misono, Y. Nishizaka, M. Kawamoto, H. Kato, Catalytic reduction of nitrogen monoxide by methane over Pd-loaded ZSM-5 zeolites; roles of acidity and Pd dispersion, Studies in Surface Science and Catalysis 105 (1997) 1501–1508.

[3] J. Long, Z. Zhang, Z. Ding, R. Ruan, Z. Li, X. Wang, Infrared study of the NO reduction by hydrocarbons over iron sites with low nuclearity: some new insight into the reaction pathway, Journal of Physical Chemistry C 114 (2010) 15713–15727.

[4] A. Baylet, C. Capdeillayre, L. Retailleau, P. Vernoux, F. Figueras, A. Giroir-Fendler, Relation between partial propene oxidation, sulphate content and selective catalytic reduction of NO_x by propene on ceria/sulphated titania, Applied Catalysis B: Environmental 96 (2010) 434–440.

[5] F. Poignant, J.L. Freysz, M. Daturi, J. Saussey, Mechanism of the selective catalytic reduction of NO in oxygen excess by propane on H–Cu–ZSM-5: formation of isocyanide species via acrylonitrile intermediate, Catalysis Today 70 (2001) 197–211.

[6] L.Q. Nguyen, C. Salim, H. Hinode, Performance of nano-sized Au/TiO_2 for selective catalytic reduction of NO_x by propene, Applied Catalysis A: General 347 (2008) 94–99.

[7] J. Li, Y. Zhu, R. Ke, J. Hao, Improvement of catalytic activity and sulfur-resistance of Ag/TiO_2–Al_2O_3 for NO reduction with propene under lean burn conditions, Applied Catalysis B: Environmental 30 (2008) 202–213.

[8] H. Imai, Y. Takei, K. Shimizu, M. Matsuda, H. Hirashima, Direct preparation of anatase TiO_2 nanotubes in porous alumina membranes, Journal of Materials Chemistry 9 (1999) 2971–2972.

[9] M. Adachi, Y. Murata, M. Harada, S. Yoshikawa, Formation of titania nanotubes with high photo-catalytic activity, Chemistry Letters 8 (2000) 942–943.

[10] T. Kasuga, M. Hiramatsu, A. Hoson, T. Sekino, K. Niihara, Formation of titanium oxide nanotube, Langmuir 14 (1998) 3160–3163.

[11] T. Kasuga, M. Hiramatsu, A. Hoson, T. Sekino, K. Niihara, Titania nanotubes prepared by chemical processing, Advanced Materials 11 (1999) 1307–1311.

[12] A. Corma, Inorganic solid acids and their use in acid-catalyzed hydrocarbon reactions, Chemical Reviews 95 (1995) 559–614.

[13] L.K. Noda, R.M. de Almeida, L.F.D. Probst, N.S. Gonçalves, Characterization of sulfated TiO_2 prepared by the sol–gel method and its catalytic activity in the n-hexane isomerization reaction, Journal of Molecular Catalysis A: Chemical 225 (2005) 39–46.

[14] S.M. Jung, P. Grange, The investigation of mechanism of SCR reaction on a $TiO_2–SO_4^{2-}$catalyst by DRIFTS, Applied Catalysis B: Environmental 27 (2000) L11–L16.

[15] N. Li, A. Wang, X. Wang, M. Zheng, R. Cheng, T. Zhang, NO reduction by CH_4 in the presence of excess O_2 over Mn/sulfated zirconia catalysts, Applied Catalysis B: Environmental 48 (2004) 259–265.

[16] R.Q. Long, M.T. Chang, R.T. Yang, Enhancement of activities by sulfation on Fe-exchanged TiO_2-pillared clay for selective catalytic reduction of NO by ammonia, Applied Catalysis B: Environmental 33 (2001) 97–107.

[17] S. Zhang, L. Li, F. Zhang, N. Guan, Influence of sulfation on the catalytic activity of Ni–ZrO_2 for NO reduction with propane in excess oxygen, Journal of Natural Gas Chemistry 14 (2005) 221–225.

[18] A. Baylet, C. Capdeillayre, L. Retailleau, P. Vernoux, F. Figueras, A. Giroir-Fendler, Relation between partial propene oxidation, sulphate content and selective catalytic reduction of NO_x by propene on ceria/sulphated titania, Applied Catalysis B: Environmental 96 (2010) 434–440.

[19] B.M. Holbrook, A. Baylet, L. Retailleau, A. Boreave, P. Vernoux, F. Figueras, A. Giroir-Fendler, Sulphated TiO_2 for selective catalytic reduction of NO_x by n-decane, Catalysis Today 176 (2011) 48–55.

[20] X. Chen, S. Cao, X. Weng, H. Wang, Z. Wu, Effects of morphology and structure of titanate supports on the performance of ceria in selective catalytic reduction of NO, Catalysis Communications 26 (2012) 178–182.

[21] L.M. Sikhwivhilu, S. Sinha Ray, N.J. Coville, Influence of bases on hydrothermal synthesis of titanate nanostructures, Applied Physics A 94 (2009) 963–973.

[22] E. Barraud, F. Bosc, D. Edwards, N. Keller, V. Keller, Gas phase photocatalytic removal of toluene effluents on sulfated titania, Journal of Catalysis 235 (2005) 318–326.

[23] J. Yu, H. Yu, C.H. Ao, S.C. Lee, J.C. Yu, W. Ho, Preparation, characterization and photocatalytic activity of in situ Fe-doped TiO_2 thin films, Thin Solid Films 496 (2006) 273–280.

[24] L. Qian, Z.L. Du, S.Y. Yang, Z.S. Jin, Raman study of titania nanotube by soft chemical process, Journal of Molecular Structure 749 (2005) 103–107.

[25] M.A. Cortes-Jacome, G. Ferrat-Torres, L.F. Flores Ortiz, C. Angeles-Chavez, E. Lopez-Salinas, J. Escobar, M.L. Mosqueira, J.A. Toledo-Antonio, In situ thermo-Raman study of titanium oxide nanotubes, Catalysis Today 126 (2007) 248–255.

[26] D.V. Bavykin, J.M. Friedrich, F.C. Walsh, Protonated titanates and TiO_2 nanostructured materials: synthesis, properties and applications, Advanced Materials 18 (2006) 2807–2824.

[27] L. Qian, Z.L. Du, S.Y. Yang, Z.S. Jin, Raman study of titania nanotube by soft chemical process, Journal of Molecular Structure 749 (2005) 103–107.

[28] X. Sun, Y. Li, Synthesis and characterization of ion-exchangeable titanate nanotubes, Chemistry—A European Journal 9 (2003) 2229–2238.

[29] D.L.A. de Faria, V. Silva, M.T. de Oliveira, Raman microspectroscopy of some iron oxides and oxyhydroxides, Journal of Raman Spectroscopy 28 (1997) 873–878.

[30] Y. Hou, H. Zheng, Z. Ding, L. Wu, Effects of sintering temperature on physicochemical properties and photocatalytic activity of titanate nanotubes modified with sulfuric acid, Powder Technology 214 (2011) 451–457.

[31] J.R. Sohn, H.J. Kim, High catalytic activity of NiO–TiO_2/SO_4^{2-} for ethylene dimerization, Journal of Catalysis 101 (1986) 428–433.

[32] M. Zhou, J. Yu, B. Cheng, H. Yu, Preparation and photocatalytic activity of Fe-doped mesoporous titanium dioxide nanocrystalline photocatalysts, Materials Chemistry and Physics 93 (2005) 159–163.

[33] J.F. Moulder, W.F. Stickle, P.E. Sobol and K.D. Bomben, Handbook of X-ray Photoelectron Spectroscopy, Physical Electronics Division, Perkin-Elmer Corporation, Eden Prairie, MN, USA, 1992.

[34] P. Zhang, S. Yin, T. Sato, Synthesis of iron-containing nitrogen-doped titania by hydrothermal method and its photocatalytic activity, Research on Chemical Intermediates 37 (2011) 479–485.

[35] L. Deng, S. Wang, D. Liu, B. Zhu, W. Huang, S. Wu, S. Zhang, Synthesis, characterization of Fe-doped TiO_2 nanotubes with high photocatalytic activity, Catalysis Letters 129 (2009) 513–518.

[36] W. Choi, A. Termin, M.R. Hoffmann, The role of metal ion dopants in quantum-sized TiO_2: correlation between photoreactivity and charge carrier recombination dynamics, Journal of Physical Chemistry 98 (1994) 13669–13679.

[37] Z. Zhang, C.C. Wang, R. Zakaria, J.Y. Ying, Role of particle size in nanocrystalline TiO_2-based photocatalysts, Journal of Physical Chemistry B 102 (1998) 10871–10878.

[38] B.S. Klose, F.C. Jentoft, R. Schlogl, I.R. Subbotina, V.B. Kazansky, Effect of Mn and Fe on the reactivity of sulfated zirconia toward H_2 and n-butane: a diffuse reflectance IR spectroscopic investigation, Langmuir 21 (2005) 10564–10572.

[39] A.L.C Pereira, S.G. Marchetti, A. Albornoz, P. Reyes, M. Oportus, Maria do Carmo Rangel, Effect of iron on the properties of sulfated zirconia, Applied Catalysis A: General 334 (2008) 187–198.

[40] F. Liu, H. He, C. Zhang, Z. Feng, L. Zheng, Y. Xie, T. Hu, Selective catalytic reduction of NO with NH_3 over iron titanate catalyst: catalytic performance and characterization, Applied Catalysis B: Environmental 96 (2010) 408–420.

[41] S.M. Kumbar, G.V. Shanbhag, F. Lefebvre, S.B. Halligudi, Heteropoly acid supported on titania as solid acid catalyst in alkylation of p-cresol with tert-butanol, Journal of Molecular Catalysis A: Chemical 256 (2006) 324–334.

[42] B.H. Davis, R.A. Keogh, S. Alerasool, D.J. Zalewski, D.E. Day, P. K. Doolin, Infrared study of pyridine adsorbed on unpromoted and promoted sulfated zirconia, Journal of Catalysis 183 (1999) 45–52.

[43] G. Busca, Spectroscopic characterization of the acid properties of metal oxide catalysts, Catalysis Today 41 (1998) 91–206.

[44] M. Zhou, J. Yu, B. Cheng, Effects of Fe-doping on the photocatalytic activity of mesoporous TiO_2 powders prepared by an ultrasonic method, Journal of Hazardous Materials 137 (2006) 1838–1847.

[45] L. Chmielarz, P. Kuśtrowski, A. Rafalska-Łasocha, R. Dziembaj, Selective oxidation of ammonia to nitrogen on transition metal containing mixed metal oxides, Applied Catalysis B: Environmental 58 (2005) 235–244.

[46] M.R. Hoffmann, S.T. Martin, W. Choi, D.W. Bahnemann, Environmental applications of semiconductor photocatalysis, Chemical Reviews 95 (1995) 69–96.

[47] E. Garcia-Bordeje, J.L. Pinilla, M.J. Lazaro, R. Moliner, J.L.G. Fierro, Role of sulphates on the mechanism of NH_3-SCR of NO at low temperatures over presulphated vanadium supported on carbon-coated monoliths, Journal of Catalysis 233 (2005) 66–175.

[48] S.T. Choo, Y.G. Lee, I.-S. Nam, S.-W. Ham, J.-B. Lee, Characteristics of V_2O_5 supported on sulfated TiO_2 for selective catalytic reduction of NO by NH_3, Applied Catalysis A: General 200 (2000) 177–188.

[49] E. Kikuchi, K. Yogo, Selective catalytic reduction of nitrogen monoxide by methane on zeolite catalysts in an oxygen-rich atmosphere, Catalysis Today 22 (1994) 73–86.

[50] M. Kantcheva, A.S. Vakkasoglu, Cobalt supported on zirconia and sulfated zirconia: II. Reactivity of adsorbed NO_x compounds toward methane, Journal of Catalysis 223 (2004) 364–371.

[51] T.K. Cheung, B.C. Gates, Sulfated zirconia and iron- and manganese-promoted sulfated zirconia: do they protonate alkanes?, Topics in Catalysis 6 (1998) 41–47